Supporting Material

The Supporting Material has two main sections, Supplemental Computations and Supplemental Methods, followed by a Supplemental Note concerning the definition of the Lyapunov exponent.

Supplemental Computations

Supplemental Computations is divided into five subsections. In Section 1 we show that the simple FN model and more complex biophysical models make qualitatively similar predictions of dynamical instability ($\lambda > 0$). In Section 2 we show that low-rate stimulation causes the FN model to fire regularly, in lock-step to the applied stimulus (cf. the irregular pattern to high-rate stimulation shown in Fig. 1). In Section 3 we show that high-rate biphasic stimulation produces instability similar to monophasic stimulation. In Section 4 we show that instability during the action potential modulates the effect of noise on the voltage-like variable x in the FN model. In Section 5 we show that dynamical instability ($\lambda > 0$) produces desynchronization of the neural firing with respect to the stimulus at late times ($t > 10/\lambda$). In Sections 6 and 7, respectively, we show that dynamical instability produces exponential interspike interval histograms and decorrelated sequential intervals at late times.

1. Dynamical instability at high rates in neural models

In this section we compute the Lyapunov exponent λ of the FN model and more complex biophysical models in response to pulse trains. The biophysical models we consider are the Hodgkin-Huxley (HH) model of the squid giant axon (Hodgkin and Huxley 1952) and the Schwarz-Eikhof (SE) model of the mammalian sciatic nerve fiber (Schwarz and Eikhof 1987). The surface (upper) and density (lower) plots of

Supplemental Fig. 1 show the Lyapunov exponent predicted by FN model for stimulus pulse amplitudes A between 0.5 and 2 times the threshold A_θ and for interpulse times T between 0.1 and 10 times the refractory time t_d. Corresponding plots for the HH and SE models are shown in Supplemental Figs. 2 and 3. Supplemental Figure 4 shows the Lyapunov exponent for all three models as a function of the stimulus pulse rate for a fixed pulse amplitude ($A/A_\theta = 1.13278$). These plots show that, like the FN model, the biophysical HH and SE models are dynamically unstable ($\lambda > 0$) at high stimulation rates, which suggests that dynamical instability at high rates is a general feature of neural excitation and refractoriness and not merely a peculiarity of the FN model. Additionally, Supplemental Fig. 5 shows that during the action potential the behavior of $|\bar{R}(t)|/|\bar{R}(0)|$ is also qualitatively similar across the three models.

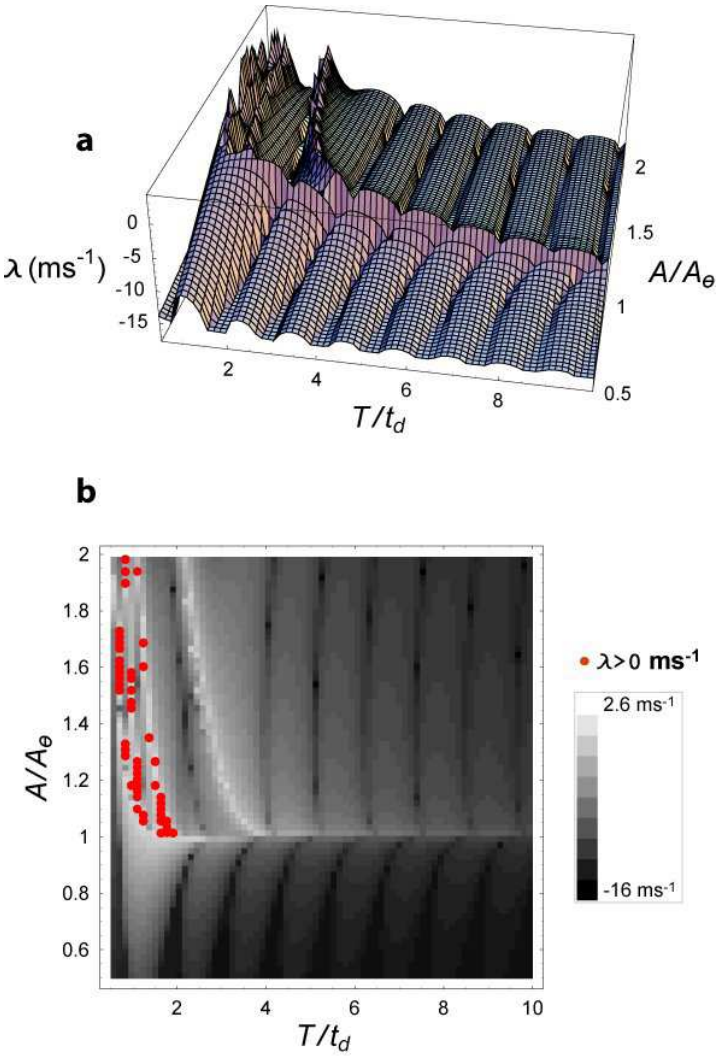

Supplemental Fig. 1. The rate and level dependence of the Lyapunov exponent of the FN model when driven by uniform pulse trains. Surface plot (a) and density plot (b) of the Lyapunov exponent of the FN model as a function of the pulse train amplitude A/A_θ and interpulse time T/t_d, where A_θ is the threshold to an isolated pulse and t_d is the nominal refractory time. In the density plot, red dots indicate $\lambda > 0$. Due to their limited resolution these plots do not necessarily capture details of the fine structure within the major peak regions. The refractory time is $t_d = 3.66$, expressed in the dimensionless units of equations (1) and (2).

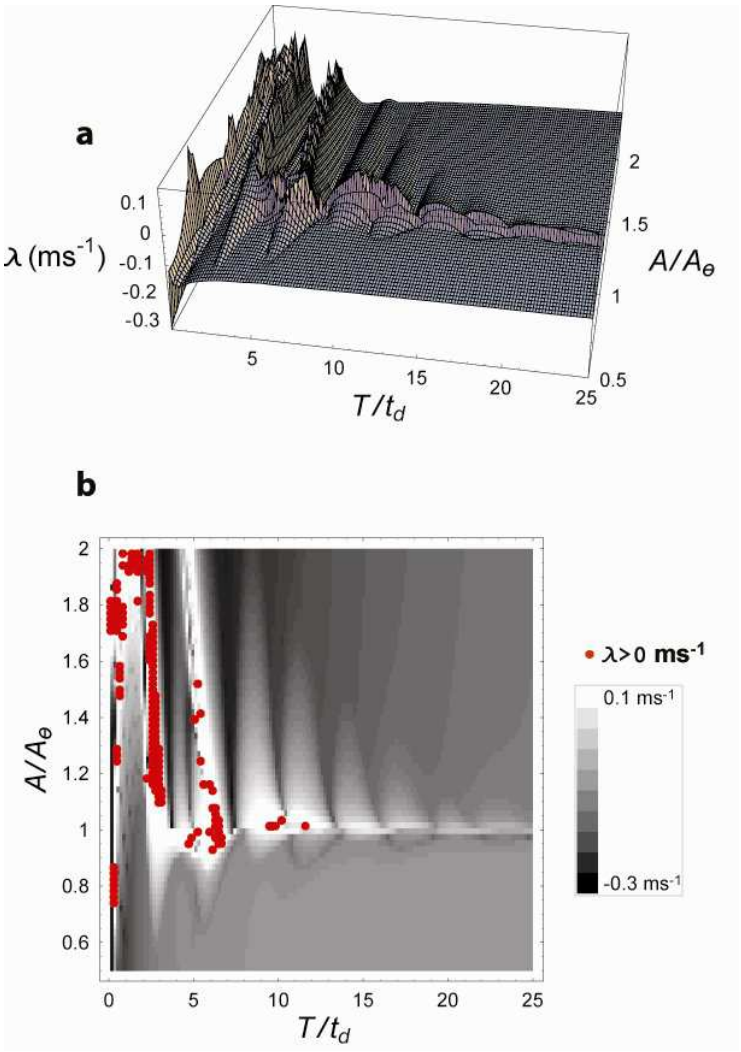

Supplemental Fig. 2. The rate and level dependence of the Lyapunov exponent of the HH model when driven by uniform pulse trains. Surface plot (a) and density plot (b) of the Lyapunov exponent of the HH model as a function of the pulse train amplitude A/A_θ and interpulse time T/t_d, where A_θ is the threshold to an isolated pulse and t_d is the nominal refractory time. In the density plot, red dots indicate $\lambda > 0$. Due to their limited resolution these plots do not necessarily capture details of the fine structure within the major peak regions. The refractory time is $t_d = 2.8$ ms.

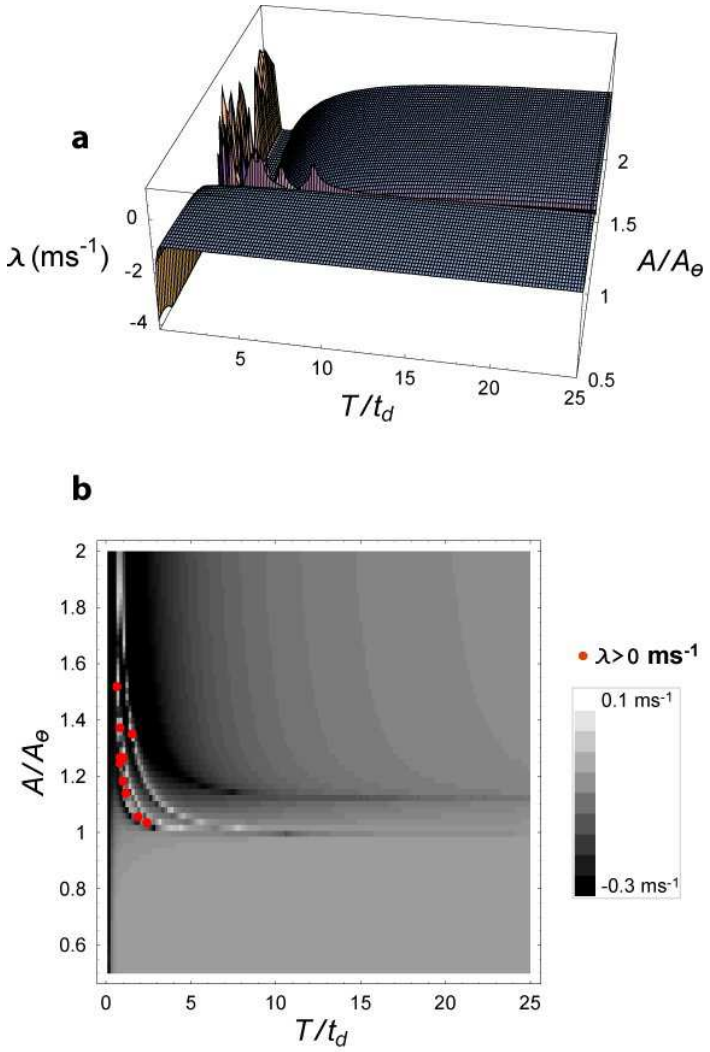

Supplemental Fig. 3. The rate and level dependence of the Lyapunov exponent of the SE model when driven by uniform pulse trains. Surface plot (a) and density plot (b) of the Lyapunov exponent of the SE model as a function of the pulse train amplitude A/A_θ and interpulse time T/t_d, where A_θ is the threshold to an isolated pulse and t_d is the nominal refractory time. In the density plot, red dots indicate $\lambda > 0$. Due to their limited resolution these plots do not necessarily capture details of the fine structure within the major peak regions. The refractory time is $t_d = 0.388$ ms.

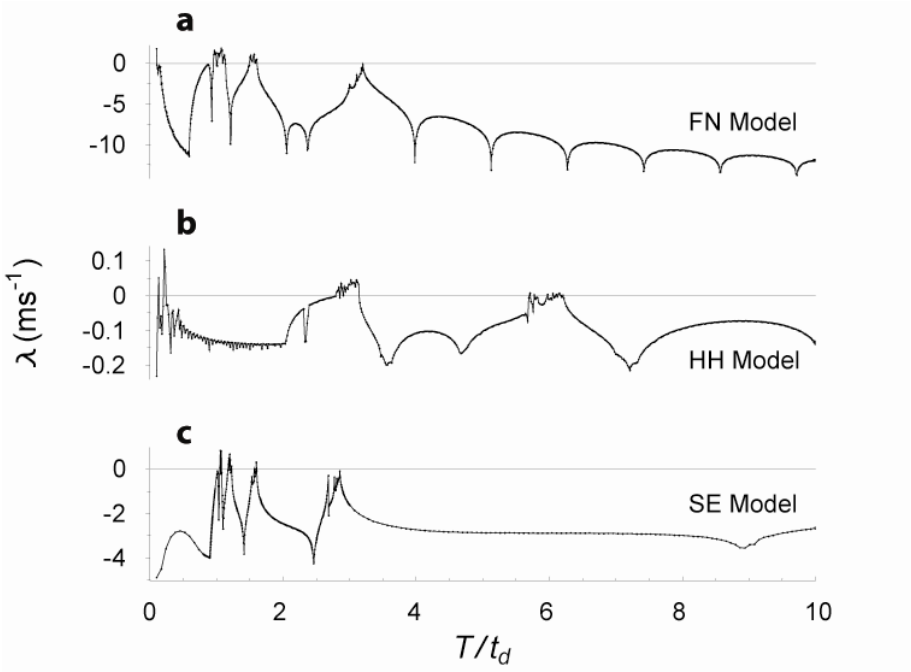

Supplemental Fig. 4. High-rate instability in the FN, HH, and SE models. Plots of Lyapunov exponent versus the interpulse time T/t_d for the FN (a), HH (b), and SE (c) models. The stimulus level of is A/A_0=1.13278 .

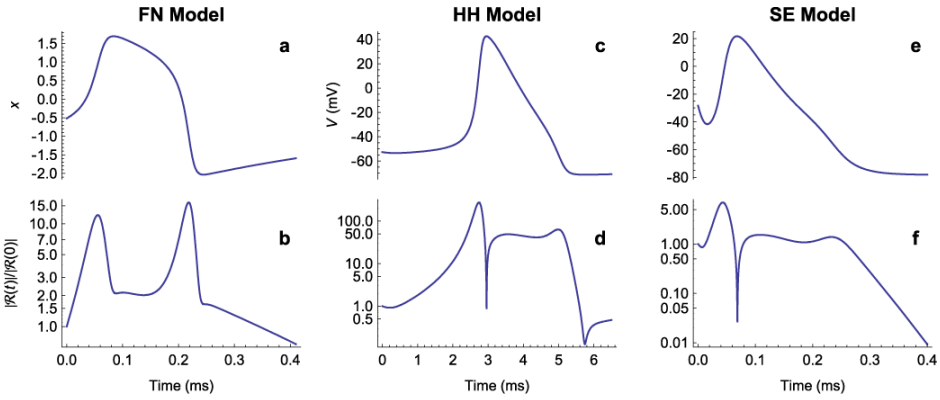

Supplemental Fig. 5. Short-term instability in the FN, HH, and SE models during the action potential. The time course of the "voltage" variable, $x(t)$, of the FN model (a) and the magnitude of the perturbation vector $|\bar{R}(t)|/|\bar{R}(0)|$ (b) in response to a brief current pulse delivered at $t = 0$. A positive slope $d(|\bar{R}(t)|/|\bar{R}(0)|)/dt > 0$ indicates short-term dynamical instability. Corresponding plots for the HH and SE model are shown in panels (c, d) and (e, f), respectively. The pulse amplitude of is A/A_0=1.13278 in all cases.

2. Regular firing at low stimulation rates in the FN model

Figure 1 of the main text shows the irregular firing pattern produced by the FN model when stimulated at 5 kHz. Supplemental Figure 6 shows that when the stimulus rate is reduced to 1 kHz the FN model fires regularly, in lock-step to the stimulus pulses.

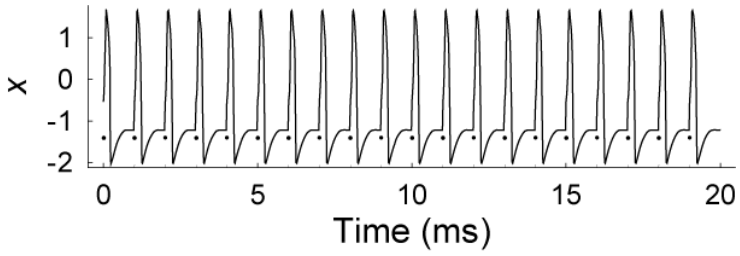

Supplemental Fig. 6. Low-rate stimulation produces dynamical stability ($\lambda < 0$) and regular firing in the FN model. The stimulus is a 1 kHz pulse train with the same amplitude as that used in Fig. 5 (A/A_0=1.12992). The timing of the individual pulses is represented by black dots. Each pulse evokes a spike. The value of the Lyapunov exponent is $\lambda \simeq -2.06$ ms^{-1} .

3. Dynamical instability produced by biphasic pulse trains in the FN model

The physiological experiments of Litvak et al. and Miller et al. used "biphasic" pulses, consisting of a brief cathodic phase followed by an anodic phase of equal duration. Monophasic and biphasic pulse trains are represented schematically in Supplemental Fig. 7a. Like stimulation with a monophasic pulse train (Supplemental Fig. 7b, black), stimulation with a biphasic pulse train produces fluctuations in the Lyapunov exponent (λ) as the stimulus period T is reduced, and, for a range of values of T , the Lyapunov exponent exceeds zero, indicating dynamical instability.

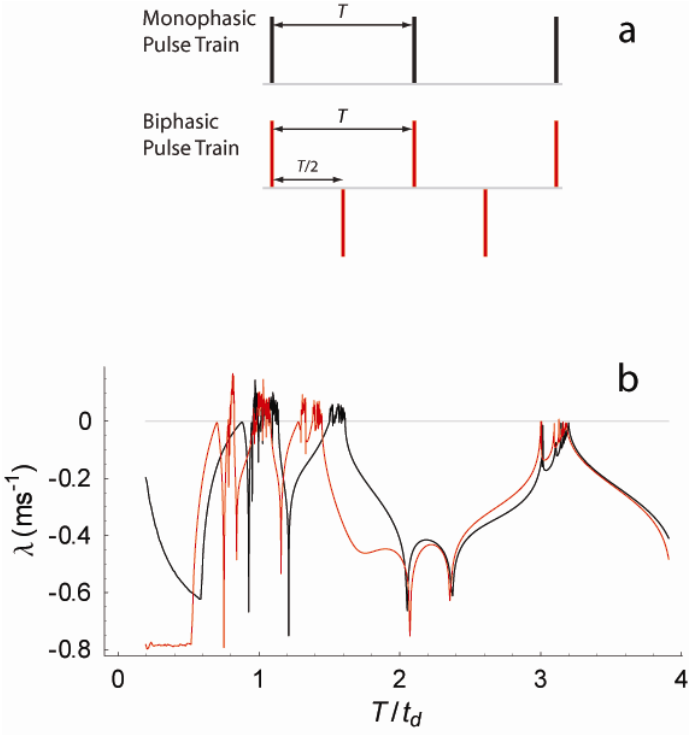

Supplemental Fig. 7a. Schematic illustration of monophasic and biphasic pulse trains. For simplicity, the negative-going pulses are placed halfway between the positive-going pulses.

Supplemental Fig. 7b. Biphasic pulse trains produce dynamical instability at high stimulation rates in the FN model. Plots of the Lyapunov exponent λ versus the fundamental period T of the stimulating biphasic pulse train (red) and the stimulating monophasic pulse train (black). The fundamental period is expressed in units of the nominal refractory time t_d.

4. Dynamical instability modulates the effect of noise during the action potential

Although the noise-forcing term that is added to the differential equation for $x'(t)$ (Equation 1) is constant, Figure 8 shows that its effect on the root-mean-square (rms) amplitude of $x(t)$ (about the mean) is modulated during the action potential by the (short-term) dynamical instability, defined as $\frac{d}{dt}\{\ln(|\,\bar{R}(t)\,|\,/\,|\,\bar{R}(0)\,|)\}$.

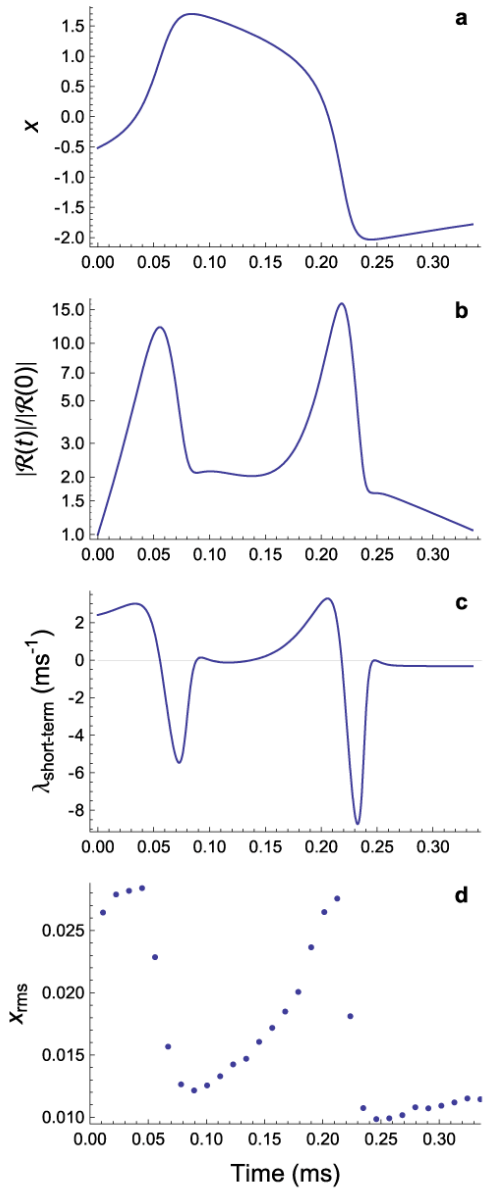

Supplemental Fig. 8. Dynamical instability modulates the effect of noise on the voltage-like variable *x*. The time evolution, $x(t)$, of the voltage-like variable of the noise-free FN model in response to a brief pulse (a), the magnitude of the perturbation vector $|\bar{R}(t)|/|\bar{R}(0)|$ (b), the short-term Lyapunov exponent defined as $\frac{d}{dt}\{\ln(|\bar{R}(t)|/|\bar{R}(0)|)\}$ (c), the rms value about the mean of the voltage-like variable (x_{rms}) of the stochastic FN model (RS=0.07) computed at the end of sequential, 0.0112 ms bins (**d**). The simulation was restarted on the noise-free solution at the beginning of each bin, so x_{rms} reflects the influence of noise during the bin rather than the cumulative effects of noise occurring in previous bins. The values of x_{rms} are averages obtained from 2000 independent realizations of the stochastic

process.

5. Dynamical instability produces desynchronization with respect to the stimulus at late times

Auditory-nerve fibers stimulated electrically at high rates typically fire synchronously for the first few spikes and then desynchronize (Litvak et al. 2001). Here we use the spike-train autocorrelation histogram to quantify degree of synchrony predicted by the noise-free FN model when stimulated at high rates. The autocorrelation histogram is computed in the same manner as the cross-correlation histogram (see Methods), but using two copies of a single spike train, as opposed to different spike trains. A value of zero indicates desynchronization with respect to the stimulus, and the significance of the fluctuations about zero is determined by comparing to the corresponding renewal process. The 1% and 99% quantiles are indicated by the gray points.

Supplemental Figure 9 (a–c) shows that dynamical instability ($\lambda > 0$) in the FN model produces renewal-like desynchronization after an initial synchronous transient. Stimulus levels were chosen to produce firing rates of approximately 50, 150 and 250 spikes/sec, which are within the physiological range of auditory-nerve fibers. As indicated by the gray bar, the synchronous transient decays over the time scale of $10/\lambda$. The addition of ongoing noise reduces the amplitude of the transient (Supplemental Fig. 10, a–c) and causes the desynchronized, renewal-like behavior to occur sooner. The gray bar indicates the time interval between $1/|\lambda|$ and $10/|\lambda|$ (absolute values are used because the noise causes the Lyapunov exponent to be negative).

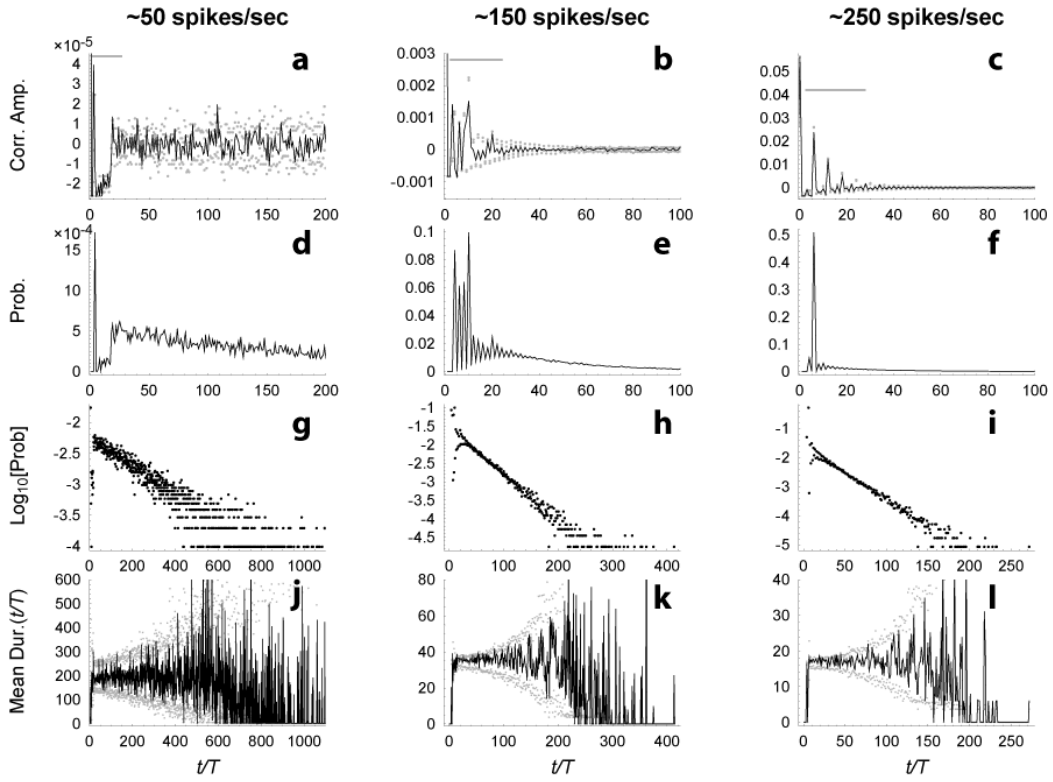

Supplemental Fig. 9. Dynamical instability produces renewal-like interval histograms at late times. The single-sided autocorrelation histogram (a–c), the interspike interval histogram with a linear vertical scale (d–f), the interspike interval histogram with logarithmic vertical scale (**g–i**), and the conditional mean interval histogram (j–l) for deterministic FN-generated spike trains with rates of approximately 50 (a, d, g, j), 150 (b, e, h, k), and 250 spikes/sec (c, f, i, l). Gray points denote the 99% and 1% quantiles for the corresponding renewal process generated by shuffling the interspike intervals. The gray bars indicate the time interval between t_λ and $10t_\lambda$, where $t_\lambda \equiv 1/\lambda$. The bin width is equal to the interpulse time T.

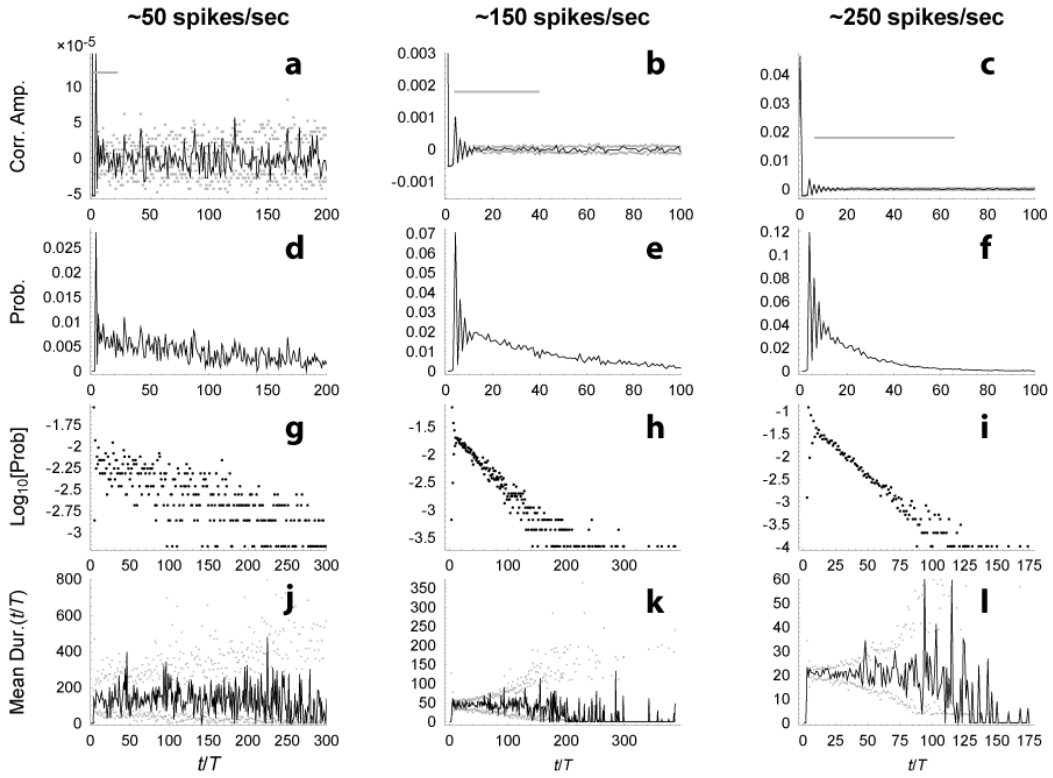

Supplemental Fig. 10. Noise smoothes interval histograms in the FN model. The single-sided cross-correlation histogram (a–c), the interspike interval histogram with linear vertical scale (d–f), the interspike interval histogram with logarithmic vertical scale (g–i), and the conditional mean interval histogram (j–l) for stochastic FN-generated spike trains with rates of approximately 50 (a, d, g, j), 150 (b, e, h, k), and 250 spikes/sec (c, f, i, l). The noise level was adjusted to produce a relative spread of $\mathrm{RS} \simeq 0.07$. Gray points denote the 99% and 1% quantiles for the corresponding renewal process generated by shuffling the interspike intervals. The gray bars indicate the time interval between $|t_\lambda|$ and $10\,|t_\lambda|$, where $t_\lambda \equiv 1/\lambda$. The Lyapunov exponent was negative for all three conditions. The bin width is equal to the interpulse time T.

6. Dynamical instability produces exponential interspike interval distributions at late times

Litvak et al. (2003) used the interspike interval histogram to characterize the temporal characteristics of the spike trains produced by auditory-nerve fibers when stimulated electrically at 5 kHz. This histogram h_k is computed from the spike train $\{t_n\}$ by forming the first-order intervals $\{\tau_n\} = \{t_{n+1} - t_n\}$ and counting the number of intervals

falling into each of k bins defined by $(k-1/2)T \le \tau < (k+1/2)T$. The histogram is normalized by dividing the number of intervals in each bin by the total number of intervals. Interval histograms from the noise-free FN model, plotted in a manner similar to figure 7 of Litvak et al. (2003), are shown in Supplemental Fig. 9, with linear (d–f) and logarithmic (g–i) vertical axes. Like most electrically stimulated fibers, the interval distributions from the noise-free FN model are exponential at late times but non-exponential at short times. Ongoing noise reduces the prominence of the non-exponential transient (Supplemental Fig. 10).

7. Dynamical instability produces decorrelated sequential intervals at late times

Litvak et al. (2003) quantified the degree of correlation between sequential interspike intervals by the conditional mean interval histogram. The conditional mean interval histogram is computed by first forming K subsequences of length J_k from the sequence of intervals $\{\tau_n\}$. These subsequences, denoted $\{\tau_{k,j}\}$, have the property that each of the J_k elements of the k^{th} subsequence is preceded by an interval of duration τ_k which falls into the k^{th} bin. From these K subsequences the conditional mean interval histogram $\overline{\tau}_k$ is constructed according to $\overline{\tau}_k = \frac{1}{J_k}\sum_{j=1}^{J_k} \tau_{k,j}$. A flat histogram implies that the probability of an interval falling into the k^{th} bin is independent of the duration of the preceding interval, and hence that sequential intervals are decorrelated. The statistical significance of deviations from flatness is evaluated by comparison to the corresponding renewal process, formed by shuffling the intervals.

Conditional mean interval histograms from the noise-free FN model, plotted in a manner similar to figure 7 of Litvak et al. (2003), are shown in Fig. 9 (j–l). Gray

points represent the 1% and 99% quantiles of the corresponding renewal process. Like most electrically stimulated fibers, the conditional mean interval histogram falls within the bounds of the corresponding renewal process at late times. This is consistent the interspike interval being independent of the preceding interval, except when the preceding interval is short. This decorrelation at late times also occurs in the presence of ongoing noise Fig. 10 (j–l).

Supplemental Methods

Here we demonstrate that the numerical methods used in this study produce estimates of the Lyapunov exponent that are robust to errors associated with finite averaging time and finite computational precision. We also demonstrate that the estimates of the Lyapunov exponent exhibit power-law convergence.

The robustness of the finding of dynamical instability in the FN model

Although the two numerical methods used in this study, the NDSolve method and the fixed-step-size Euler method, may make different predictions about a particular solution at late times, even when started with nominally identical initial conditions, we demonstrate that they nevertheless yield similar estimates of the Lyapunov exponent.

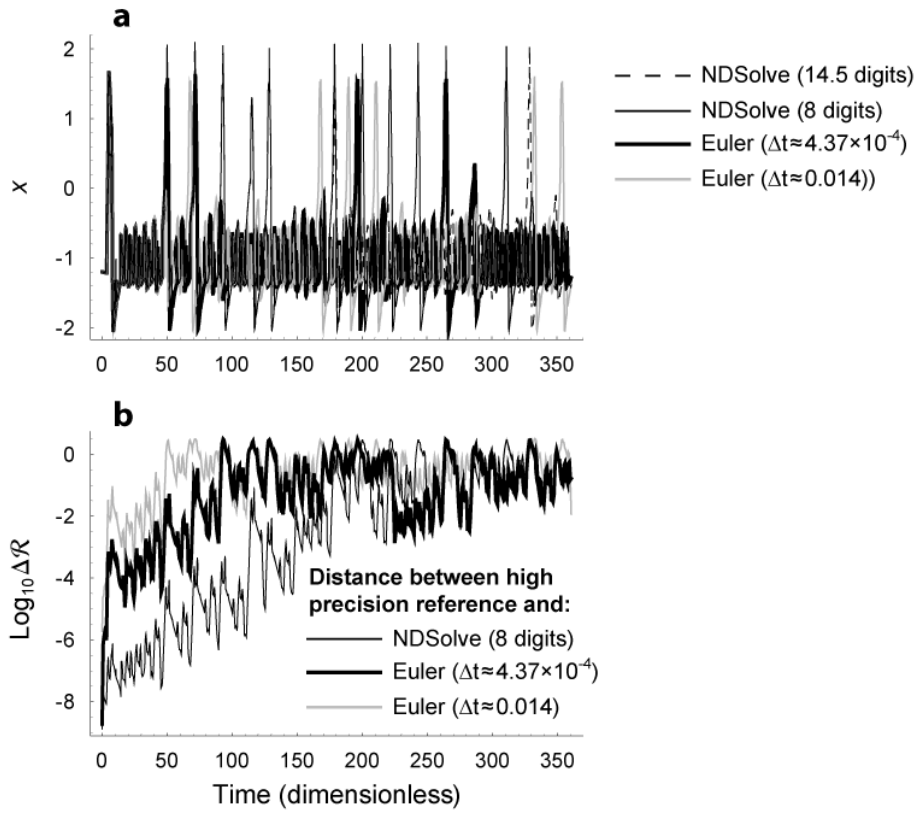

Supplemental Fig. 11. Lower precision solutions diverge from the high-precision solution at similar rates. (a) Time evolution of the excitation variable, x, of the FitzHugh-Nagumo system when driven by a near threshold pulse train (A/A_θ=1.13278) at a rate corresponding to 5 kHz ($T \simeq 3.578$). The different curves correspond to different solution methods (see figure legend). (b) The time evolution of the phase-plane distance between a high-precision solution (14.5 decimal digits) and three lower precision solutions (see figure legend).

Supplemental Figure 11a shows predictions of the voltage-like variable $x(t)$ generated by: 1) the NDSolve algorithm with a high numerical precision setting of 14.5 decimal digits (dashed black line), 2) the NDSolve algorithm with a precision setting of 8 digits that is used for the noise-free simulations in the main text (thin black line), 3) the Euler method with a small step size (thick black line), and 4) the Euler method with the larger step size (gray line) used for the stochastic simulations in the main text. The predictions visually overlap during the first approximately $t \simeq 45$ time units, corresponding to the first 12 pulses, after which the prediction of the larger step-size Euler method noticeably diverges from the other solutions. Later

at $t \simeq 70$ the smaller step-size Euler prediction diverges from the NDSolve solutions. Around $t = 180$ or the 50th pulse, the less precise NDSolve solution diverges from the higher precision NDSolve solution. This behavior is consistent with dynamical instability magnifying the effects of computational error and imprecision.

Supplemental Figure 11b plots the distance $(\Delta \mathsf{R})$ in the phase-plane between the high-precision NDSolve solution and the three lower precision solutions. Consistent with Supplemental Fig. 11a, the phase-plane distance between each of the lower precision solutions and the reference solution increases linearly (on a log scale) as the simulation progresses, with the distance eventually approaching unity (or zero on a log scale). This maximum separation is determined by the width of the attractor in phase space (Fig. 2 of main text). The similar exponential rate of separation of the solutions suggests that the three methods, though differing in their precision, may produce similar estimates of the Lyapunov exponent λ.

Supplemental Figure 12a shows the estimate of the Lyapunov exponent for these three methods as a function of the stimulus duration. The Lyapunov exponent was estimated by solving the FN equations (1) and (2) along with the variational equations (5), as described in the Methods. The total stimulus duration is $t_{total} = 200T + 5NT$, where $T \simeq 3.578$ is the interpulse time. The responses to the initial 200 pulses were discarded to minimize the influence of transients. Five estimates of λ were then made based on the remaining five stimulus segments of length NT. Error bars indicate the standard deviation of the five estimates of the less precise Euler method. This plot shows that even the least precise Euler method produces within 50 time units (14 pulses) an estimate that is significantly greater than zero. The estimates for the later times, along with error bars for all the methods, are shown in Fig. 12b–d. These data suggest that the estimate of the Lyapunov exponent

based on the least precise Euler method converges to a value that is somewhat less than that predicted by the more precise NDSolve algorithm, but that decreasing the step size of the Euler method to $\Delta t = 4.37 \times 10^{-4}$ improves the accuracy of the estimate.

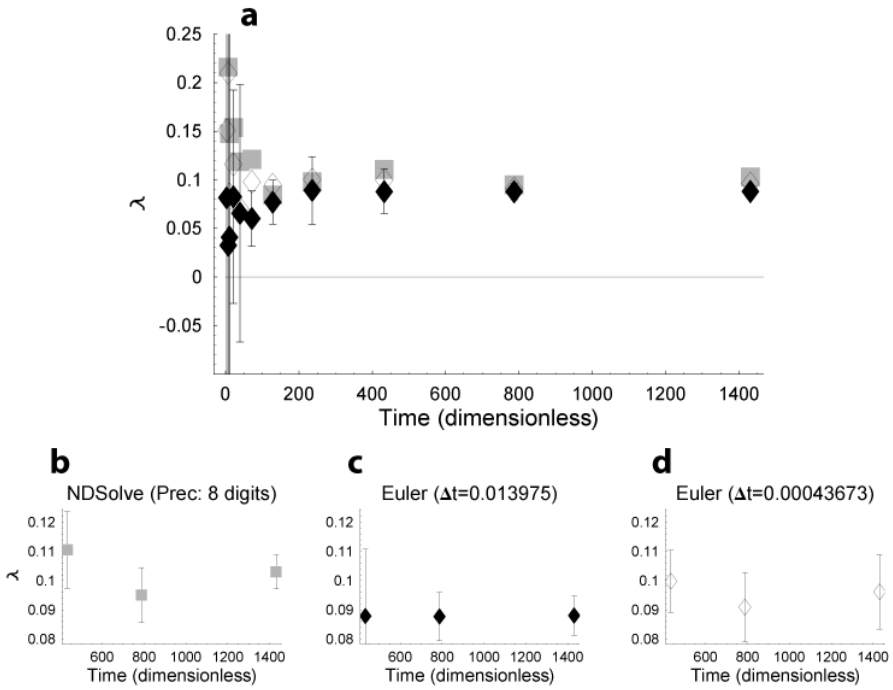

Supplemental Fig. 12. Different solution methods produce similar estimates of the Lyapunov exponent. (a) The mean estimate of the Lyapunov exponent versus the duration of a 5 kHz near threshold (A/A_0=1.13278) pulse train. The different symbols correspond to different solution methods, as in Supplemental Fig. 11. Black diamonds, representing the least precise method, are accompanied by error bars that indicate the standard deviation of estimates based on five sequential pulse trains of duration NT. Panels **b–c** show the Lyapunov exponent estimate versus t at late times, with error bars indicating the standard deviation of five sequential estimates.

While the different procedures appear to converge on slightly different values of λ, the rate at which the estimates converge to these different values is similar. This convergence rate is illustrated in Supplemental Fig. 13 which plots, on logarithmic axes, the standard deviation of the Lyapunov exponent estimate versus the simulation duration t. The approximately linear behavior, with common slopes across methods, suggests that the methods have similar power-law convergence rates.

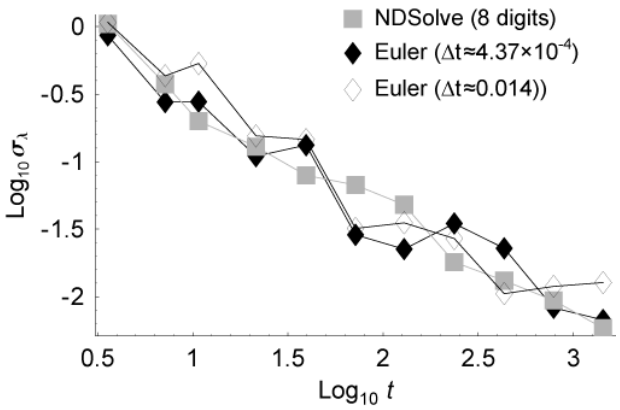

Supplemental Fig. 13. Variability of the Lyapunov exponent estimate decreases with averaging time for three solution algorithms. The logarithm of the standard deviation of the Lyapunov exponent estimate ($\mathrm{Log}_{10}\sigma_\lambda$) as a function of the logarithm of the stimulus duration ($\mathrm{Log}_{10}t$) for three solution methods (see figure legend).

We now further investigate the effects of numerical precision on the estimates using the NDSolve method. The NDSolve method uses an algorithm that adaptively varies the step size in order to achieve the precision goal set by the user. For sufficiently high precision settings, typically above 8 decimal digits, computations must be carried out with a precision greater than the standard machine precision of approximately 16 decimal digits. This higher precision is achieved in *Mathematica* by using arbitrary precision numbers at the expense of longer computation time (Wolfram 1996). Supplemental Figure 14 shows the estimates of λ for $200+5\times300=1700$ pulses for a range of precision settings. Because the mean of every estimate falls within the confidence interval of all the other estimates, we conclude that the finding of instability ($\lambda>0$) is robust to errors in computational precision.

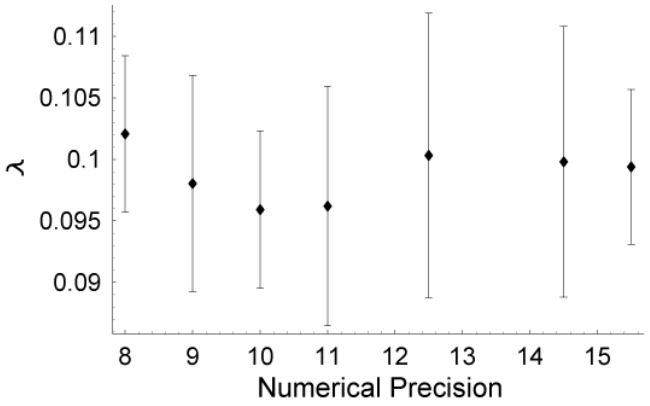

Supplemental Fig. 14. The estimate of the Lyapunov exponent is robust to increases in computational precision. The mean of five estimates of the Lyapunov exponent plotted as a function of the numerical precision setting of the NDSolve algorithm. With a numerical precision of *p*, the local error is less than $10^{-p} + |X_i| 10^{-p}$, where $|X_i|$ is the absolute value of the i^{th} independent variable (Wolfram 1996). The Lyapunov exponent estimates were obtained from pulse trains of duration $NT = 200T + 5 \times 300T = 1700$. The responses to the initial 200 pulses were discarded, and estimates were then formed based on the responses to each of the five subsequent segments consisting of 300 pulses. The error bars represent the standard deviation of these estimates. The stimulus conditions are the same as in Supplemental Figs. 11–13.

In summary, we have shown that for a typical near threshold, high-rate condition both the NDSolve method and the fixed-step-size Euler method predict dynamical instability $(\lambda > 0)$, and further that this prediction of instability is robust to the errors associated with the finite duration and the finite precision of the calculations.

Supplemental Note

For the driven FN model the phase space is, strictly speaking, three dimensional, and thus there are three Lyapunov exponents, one for each dimension (Eckmann and Ruelle 1985). The evolution in this third dimension is given trivially by the equation $t'(t) = 1$ (Strogatz 1994). Along this time axis, there is neither contraction nor stretching, and hence one of the three exponents is identically zero always. Further,

because the system is dissipative, the volume of a small cube of initial conditions will shrink under the influence of the flow. The long-term rate of change in the volume is directly proportional to the sum of the Lyapunov exponents (Eckmann and Ruelle 1985), and, because this volume is contracting, the sum of the exponents must be less than zero, thus when one of the two non-zero exponents is positive the other must be negative. Furthermore, an arbitrary perturbation vector, under the influence of the flow, will seek out the direction of either growth or of slowest contraction (Wolf et al. 1985), thus, the exponent determined by solving the variational equations corresponds to the positive exponent, if there is one, or to the negative exponent which is closest to zero. This exponent we refer to as "the Lyapunov exponent."

References

Eckmann J-P, and Ruelle D. Ergodic theory of chaos and strange attractors. Rev Mod Phys 57: 617-656, 1985.

Hodgkin AL, and Huxley AF. A quantitative description of membrane current and its application to conduction and excitation in nerve. J Physiol (Lond) 117: 500-544, 1952.

Litvak LM, Delgutte B, and Eddington DK. Auditory-nerve fiber responses to electric stimulation: Modulated and unmodulated pulse trains. J Acoust Soc Am 110: 368-379, 2001.

Litvak LM, Smith ZM, Delgutte B, and Eddington DK. Desynchronization of electrically evoked auditory-nerve activity by high-frequency pulse trains of long duration. J Acoust Soc Am 114: 2066-2078, 2003.

Schwarz JR, and Eikhof G. Na currents and action potentials in rat myelinated nerve fibres at 20 and 37 degrees C. Pflugers Arch 409: 569-577, 1987.

Strogatz SH. Nonlinear Dynamics and Chaos. Addison-Wesley, 1994.

Wolf A, Swift JB, Swinney HL, and Vastano JA. Determining Lyapunov exponents from a time series. Physica D 16: 285-317, 1985.

Wolfram S. The Mathematica Book. Wolfram Media/Cambridge University Press, 1996.

Supporting Material

The Supporting Material has two main sections, Supplemental Computations and Supplemental Methods, followed by a Supplemental Note concerning the definition of the Lyapunov exponent.

Supplemental Computations

Supplemental Computations is divided into five subsections. In Section 1 we show that the simple FN model and more complex biophysical models make qualitatively similar predictions of dynamical instability ($\lambda > 0$). In Section 2 we show that low-rate stimulation causes the FN model to fire regularly, in lock-step to the applied stimulus (cf. the irregular pattern to high-rate stimulation shown in Fig. 1). In Section 3 we show that high-rate biphasic stimulation produces instability similar to monophasic stimulation. In Section 4 we show that instability during the action potential modulates the effect of noise on the voltage-like variable x in the FN model. In Section 5 we show that dynamical instability ($\lambda > 0$) produces desynchronization of the neural firing with respect to the stimulus at late times ($t > 10/\lambda$). In Sections 6 and 7, respectively, we show that dynamical instability produces exponential interspike interval histograms and decorrelated sequential intervals at late times.

1. Dynamical instability at high rates in neural models

In this section we compute the Lyapunov exponent λ of the FN model and more complex biophysical models in response to pulse trains. The biophysical models we consider are the Hodgkin-Huxley (HH) model of the squid giant axon (Hodgkin and Huxley 1952) and the Schwarz-Eikhof (SE) model of the mammalian sciatic nerve fiber (Schwarz and Eikhof 1987). The surface (upper) and density (lower) plots of

Supplemental Fig. 1 show the Lyapunov exponent predicted by FN model for stimulus pulse amplitudes A between 0.5 and 2 times the threshold A_θ and for interpulse times T between 0.1 and 10 times the refractory time t_d. Corresponding plots for the HH and SE models are shown in Supplemental Figs. 2 and 3. Supplemental Figure 4 shows the Lyapunov exponent for all three models as a function of the stimulus pulse rate for a fixed pulse amplitude ($A/A_\theta = 1.13278$). These plots show that, like the FN model, the biophysical HH and SE models are dynamically unstable ($\lambda > 0$) at high stimulation rates, which suggests that dynamical instability at high rates is a general feature of neural excitation and refractoriness and not merely a peculiarity of the FN model. Additionally, Supplemental Fig. 5 shows that during the action potential the behavior of $|\overline{\mathcal{R}}(t)|/|\overline{\mathcal{R}}(0)|$ is also qualitatively similar across the three models.

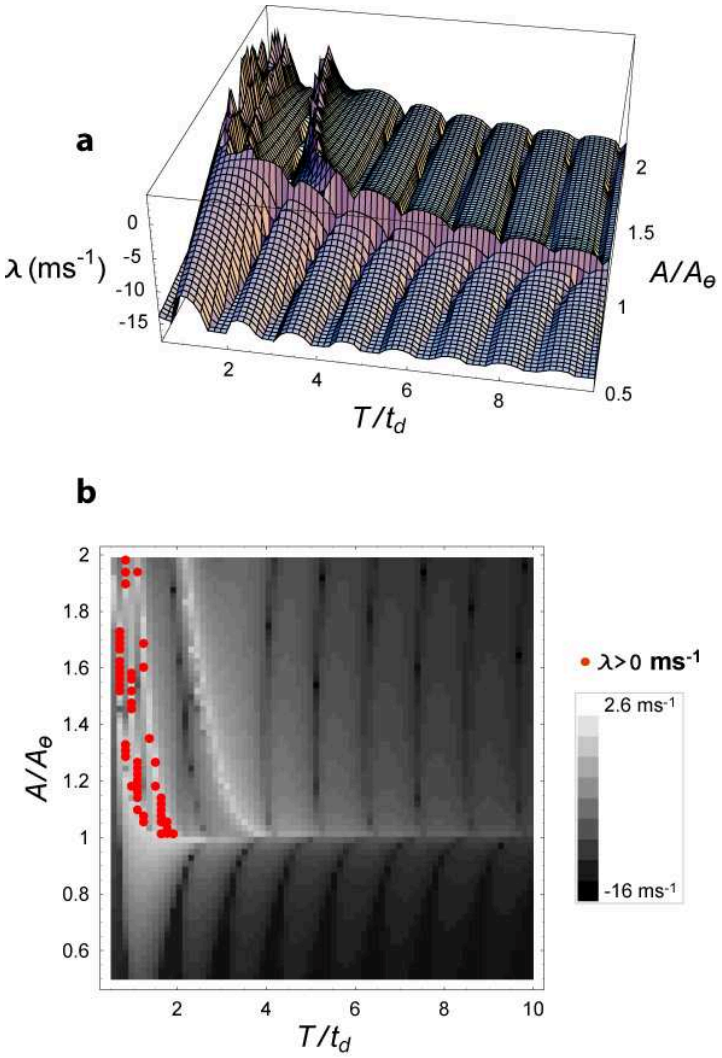

Supplemental Fig. 1. The rate and level dependence of the Lyapunov exponent of the FN model when driven by uniform pulse trains. Surface plot (a) and density plot (b) of the Lyapunov exponent of the FN model as a function of the pulse train amplitude A/A_θ and interpulse time T/t_d, where A_θ is the threshold to an isolated pulse and t_d is the nominal refractory time. In the density plot, red dots indicate $\lambda > 0$. Due to their limited resolution these plots do not necessarily capture details of the fine structure within the major peak regions. The refractory time is $t_d = 3.66$, expressed in the dimensionless units of equations (1) and (2).

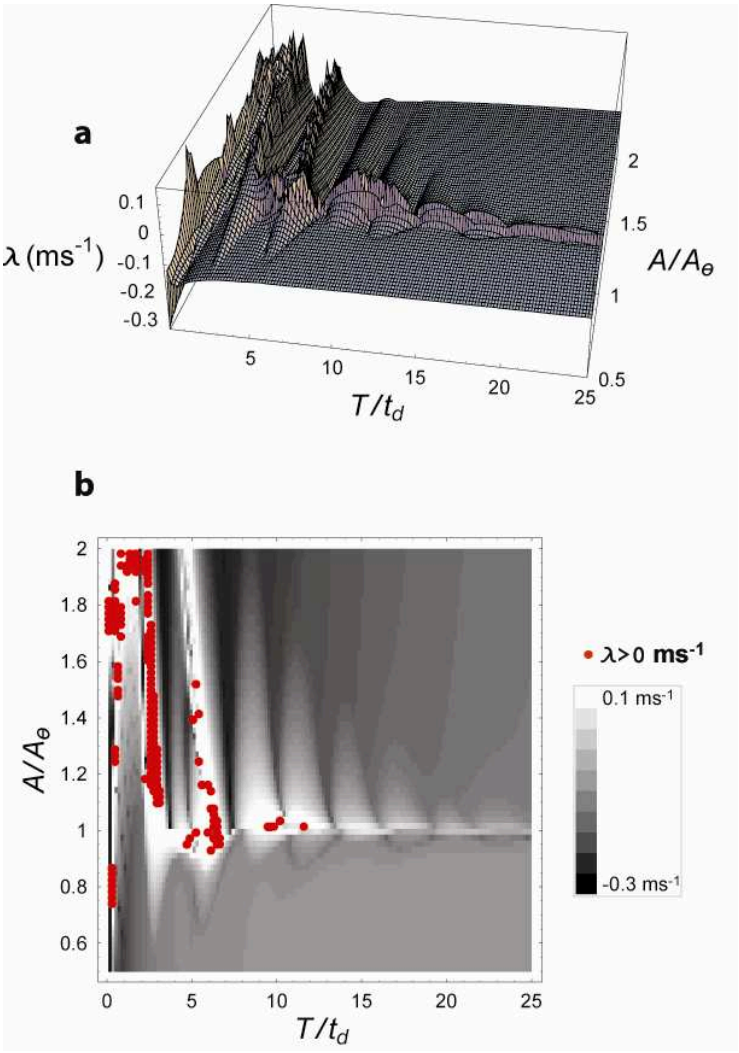

Supplemental Fig. 2. The rate and level dependence of the Lyapunov exponent of the HH model when driven by uniform pulse trains. Surface plot (a) and density plot (b) of the Lyapunov exponent of the HH model as a function of the pulse train amplitude A/A_θ and interpulse time T/t_d, where A_θ is the threshold to an isolated pulse and t_d is the nominal refractory time. In the density plot, red dots indicate $\lambda > 0$. Due to their limited resolution these plots do not necessarily capture details of the fine structure within the major peak regions. The refractory time is $t_d = 2.8$ ms.

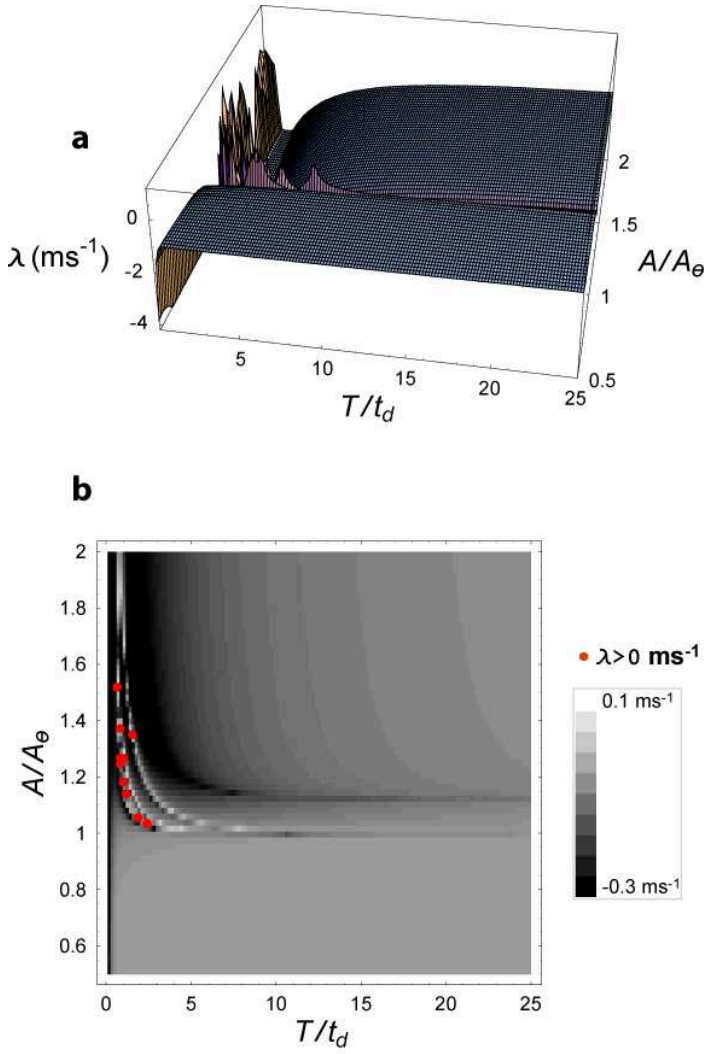

Supplemental Fig. 3. The rate and level dependence of the Lyapunov exponent of the SE model when driven by uniform pulse trains. Surface plot (a) and density plot (b) of the Lyapunov exponent of the SE model as a function of the pulse train amplitude A/A_θ and interpulse time T/t_d, where A_θ is the threshold to an isolated pulse and t_d is the nominal refractory time. In the density plot, red dots indicate $\lambda > 0$. Due to their limited resolution these plots do not necessarily capture details of the fine structure within the major peak regions. The refractory time is $t_d = 0.388$ ms.

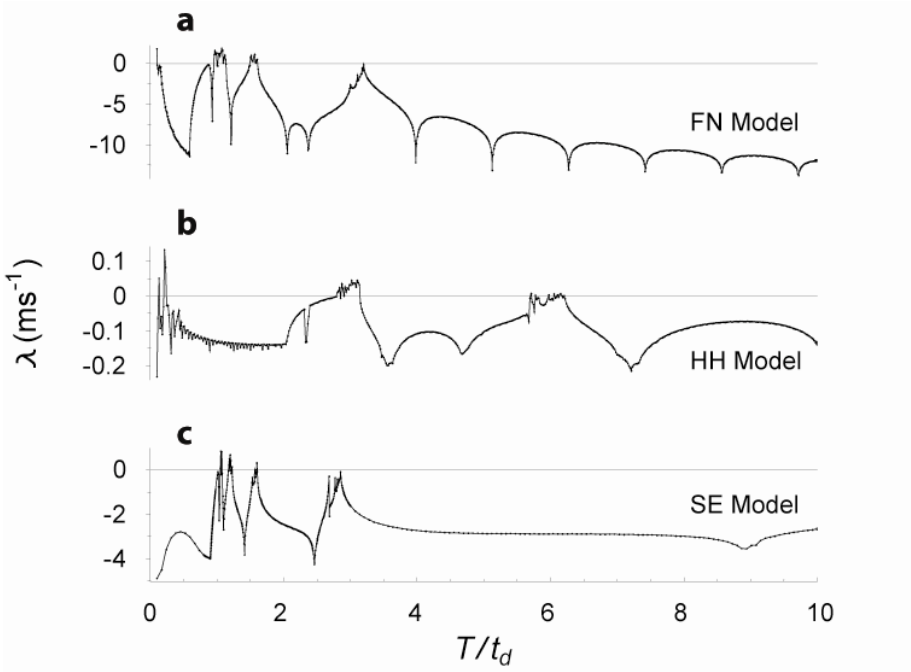

Supplemental Fig. 4. High-rate instability in the FN, HH, and SE models. Plots of Lyapunov exponent versus the interpulse time T/t_d for the FN (a), HH (b), and SE (c) models. The stimulus level of is A/A_0=1.13278 .

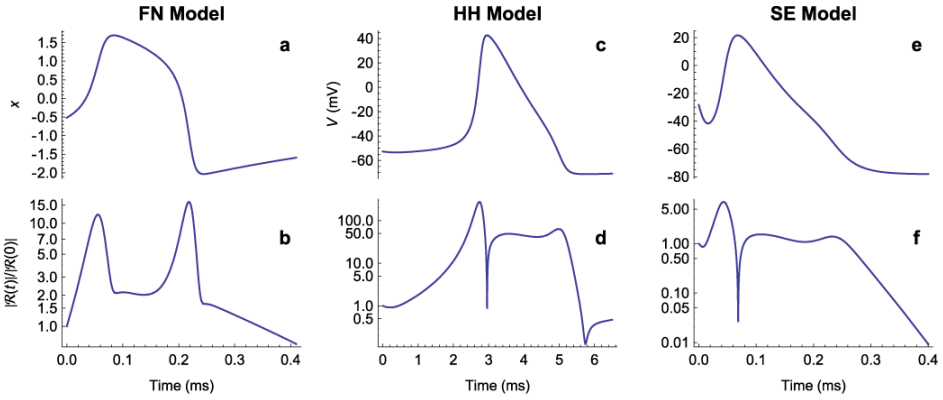

Supplemental Fig. 5. Short-term instability in the FN, HH, and SE models during the action potential. The time course of the "voltage" variable, $x(t)$, of the FN model (a) and the magnitude of the perturbation vector $|\overline{\mathcal{R}}(t)|/|\overline{\mathcal{R}}(0)|$ (b) in response to a brief current pulse delivered at $t = 0$. A positive slope $d(|\overline{\mathcal{R}}(t)|/|\overline{\mathcal{R}}(0)|)/dt > 0$ indicates short-term dynamical instability. Corresponding plots for the HH and SE model are shown in panels (c, d) and (e, f), respectively. The pulse amplitude of is A/A_0=1.13278 in all cases.

2. Regular firing at low stimulation rates in the FN model

Figure 1 of the main text shows the irregular firing pattern produced by the FN model when stimulated at 5 kHz. Supplemental Figure 6 shows that when the stimulus rate is reduced to 1 kHz the FN model fires regularly, in lock-step to the stimulus pulses.

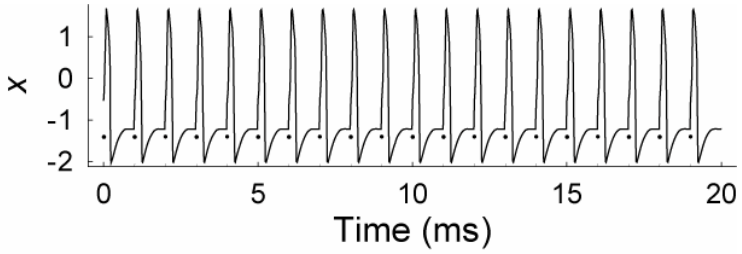

Supplemental Fig. 6. Low-rate stimulation produces dynamical stability ($\lambda < 0$) and regular firing in the FN model. The stimulus is a 1 kHz pulse train with the same amplitude as that used in Fig. 5 (A/A_0=1.12992). The timing of the individual pulses is represented by black dots. Each pulse evokes a spike. The value of the Lyapunov exponent is $\lambda \simeq -2.06$ ms^{-1} .

3. Dynamical instability produced by biphasic pulse trains in the FN model

The physiological experiments of Litvak et al. and Miller et al. used "biphasic" pulses, consisting of a brief cathodic phase followed by an anodic phase of equal duration. Monophasic and biphasic pulse trains are represented schematically in Supplemental Fig. 7a. Like stimulation with a monophasic pulse train (Supplemental Fig. 7b, black), stimulation with a biphasic pulse train produces fluctuations in the Lyapunov exponent (λ) as the stimulus period T is reduced, and, for a range of values of T , the Lyapunov exponent exceeds zero, indicating dynamical instability.

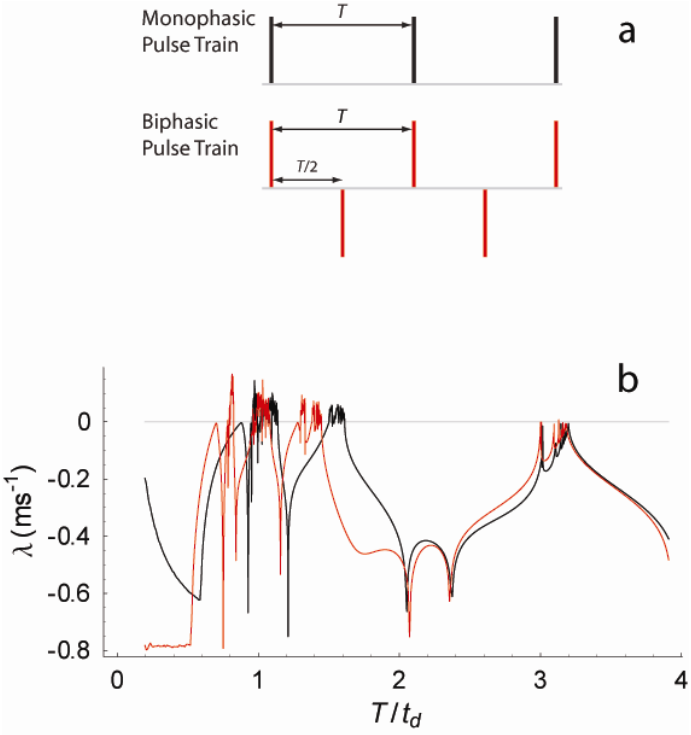

Supplemental Fig. 7a. Schematic illustration of monophasic and biphasic pulse trains. For simplicity, the negative-going pulses are placed halfway between the positive-going pulses.

Supplemental Fig. 7b. Biphasic pulse trains produce dynamical instability at high stimulation rates in the FN model. Plots of the Lyapunov exponent λ versus the fundamental period T of the stimulating biphasic pulse train (red) and the stimulating monophasic pulse train (black). The fundamental period is expressed in units of the nominal refractory time t_d.

4. Dynamical instability modulates the effect of noise during the action potential

Although the noise-forcing term that is added to the differential equation for $x'(t)$ (Equation 1) is constant, Figure 8 shows that its effect on the root-mean-square (rms) amplitude of $x(t)$ (about the mean) is modulated during the action potential by the (short-term) dynamical instability, defined as $\frac{d}{dt}\{\ln(|\overline{\mathcal{R}}(t)|/|\overline{\mathcal{R}}(0)|)\}$.

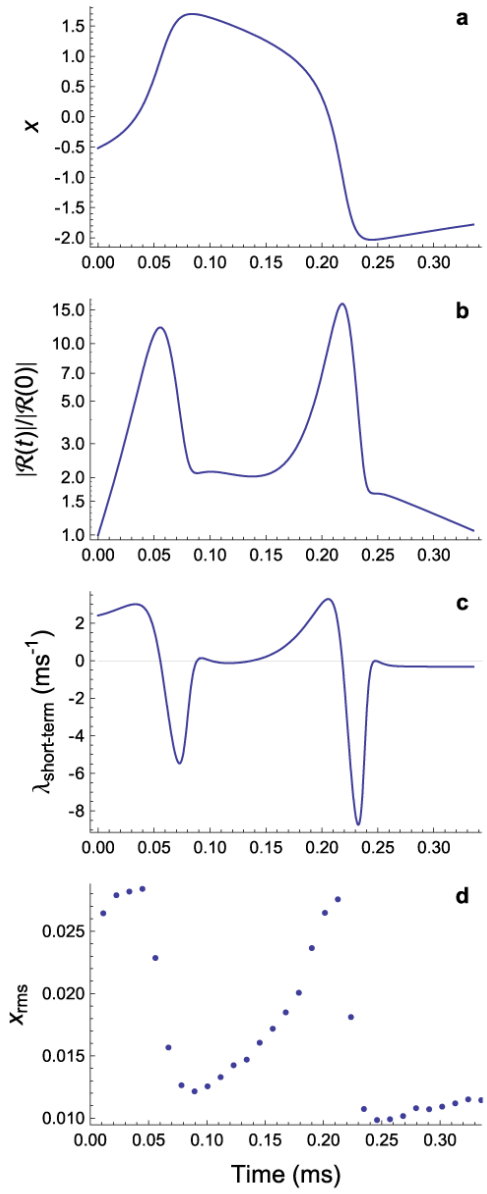

Supplemental Fig. 8. Dynamical instability modulates the effect of noise on the voltage-like variable *x*. The time evolution, $x(t)$, of the voltage-like variable of the noise-free FN model in response to a brief pulse (a), the magnitude of the perturbation vector $|\overline{\mathcal{R}}(t)|/|\overline{\mathcal{R}}(0)|$ (b), the short-term Lyapunov exponent defined as $\frac{d}{dt}\{\ln(|\overline{\mathcal{R}}(t)|/|\overline{\mathcal{R}}(0)|)\}$ (c), the rms value about the mean of the voltage-like variable (x_{rms}) of the stochastic FN model (RS=0.07) computed at the end of sequential, 0.0112 ms bins (**d**). The simulation was restarted on the noise-free solution at the beginning of each bin, so x_{rms} reflects the influence of noise during the bin rather than the cumulative effects of noise occurring in previous bins. The values of x_{rms} are averages obtained from 2000 independent realizations of the stochastic

process.

5. Dynamical instability produces desynchronization with respect to the stimulus at late times

Auditory-nerve fibers stimulated electrically at high rates typically fire synchronously for the first few spikes and then desynchronize (Litvak et al. 2001). Here we use the spike-train autocorrelation histogram to quantify degree of synchrony predicted by the noise-free FN model when stimulated at high rates. The autocorrelation histogram is computed in the same manner as the cross-correlation histogram (see Methods), but using two copies of a single spike train, as opposed to different spike trains. A value of zero indicates desynchronization with respect to the stimulus, and the significance of the fluctuations about zero is determined by comparing to the corresponding renewal process. The 1% and 99% quantiles are indicated by the gray points.

Supplemental Figure 9 (a–c) shows that dynamical instability ($\lambda > 0$) in the FN model produces renewal-like desynchronization after an initial synchronous transient. Stimulus levels were chosen to produce firing rates of approximately 50, 150 and 250 spikes/sec, which are within the physiological range of auditory-nerve fibers. As indicated by the gray bar, the synchronous transient decays over the time scale of $10/\lambda$. The addition of ongoing noise reduces the amplitude of the transient (Supplemental Fig. 10, a–c) and causes the desynchronized, renewal-like behavior to occur sooner. The gray bar indicates the time interval between $1/|\lambda|$ and $10/|\lambda|$ (absolute values are used because the noise causes the Lyapunov exponent to be negative).

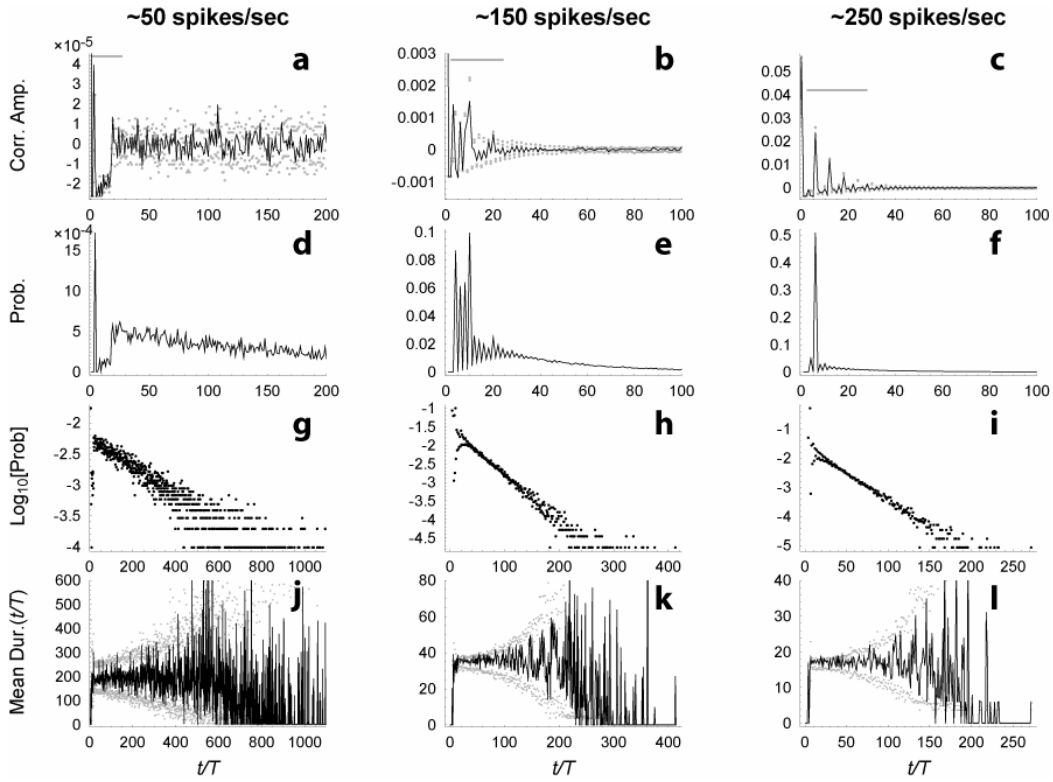

Supplemental Fig. 9. Dynamical instability produces renewal-like interval histograms at late times. The single-sided autocorrelation histogram (a–c), the interspike interval histogram with a linear vertical scale (d–f), the interspike interval histogram with logarithmic vertical scale (**g–i**), and the conditional mean interval histogram (j–l) for deterministic FN-generated spike trains with rates of approximately 50 (a, d, g, j), 150 (b, e, h, k), and 250 spikes/sec (c, f, i, l). Gray points denote the 99% and 1% quantiles for the corresponding renewal process generated by shuffling the interspike intervals. The gray bars indicate the time interval between t_λ and $10t_\lambda$, where $t_\lambda \equiv 1/\lambda$. The bin width is equal to the interpulse time T.

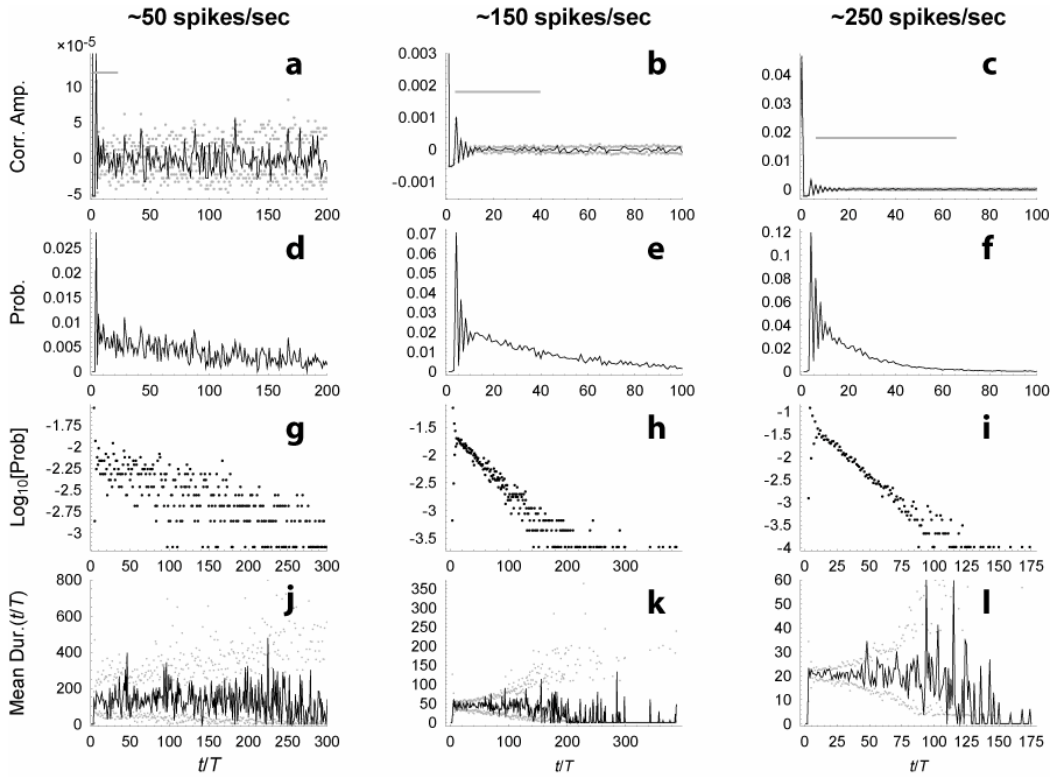

Supplemental Fig. 10. Noise smoothes interval histograms in the FN model. The single-sided cross-correlation histogram (a–c), the interspike interval histogram with linear vertical scale (d–f), the interspike interval histogram with logarithmic vertical scale (g–i), and the conditional mean interval histogram (j–l) for stochastic FN-generated spike trains with rates of approximately 50 (a, d, g, j), 150 (b, e, h, k), and 250 spikes/sec (c, f, i, l). The noise level was adjusted to produce a relative spread of $\mathrm{RS} \simeq 0.07$. Gray points denote the 99% and 1% quantiles for the corresponding renewal process generated by shuffling the interspike intervals. The gray bars indicate the time interval between $|t_\lambda|$ and $10\,|t_\lambda|$, where $t_\lambda \equiv 1/\lambda$. The Lyapunov exponent was negative for all three conditions. The bin width is equal to the interpulse time T.

6. Dynamical instability produces exponential interspike interval distributions at late times

Litvak et al. (2003) used the interspike interval histogram to characterize the temporal characteristics of the spike trains produced by auditory-nerve fibers when stimulated electrically at 5 kHz. This histogram h_k is computed from the spike train $\{t_n\}$ by forming the first-order intervals $\{\tau_n\} = \{t_{n+1} - t_n\}$ and counting the number of intervals

falling into each of k bins defined by $(k-1/2)T \le \tau < (k+1/2)T$. The histogram is normalized by dividing the number of intervals in each bin by the total number of intervals. Interval histograms from the noise-free FN model, plotted in a manner similar to figure 7 of Litvak et al. (2003), are shown in Supplemental Fig. 9, with linear (d–f) and logarithmic (g–i) vertical axes. Like most electrically stimulated fibers, the interval distributions from the noise-free FN model are exponential at late times but non-exponential at short times. Ongoing noise reduces the prominence of the non-exponential transient (Supplemental Fig. 10).

7. Dynamical instability produces decorrelated sequential intervals at late times

Litvak et al. (2003) quantified the degree of correlation between sequential interspike intervals by the conditional mean interval histogram. The conditional mean interval histogram is computed by first forming K subsequences of length J_k from the sequence of intervals $\{\tau_n\}$. These subsequences, denoted $\{\tau_{k,j}\}$, have the property that each of the J_k elements of the k^{th} subsequence is preceded by an interval of duration τ_k which falls into the k^{th} bin. From these K subsequences the conditional mean interval histogram $\overline{\tau}_k$ is constructed according to $\overline{\tau}_k = \frac{1}{J_k}\sum_{j=1}^{J_k} \tau_{k,j}$. A flat histogram implies that the probability of an interval falling into the k^{th} bin is independent of the duration of the preceding interval, and hence that sequential intervals are decorrelated. The statistical significance of deviations from flatness is evaluated by comparison to the corresponding renewal process, formed by shuffling the intervals.

Conditional mean interval histograms from the noise-free FN model, plotted in a manner similar to figure 7 of Litvak et al. (2003), are shown in Fig. 9 (j–l). Gray

points represent the 1% and 99% quantiles of the corresponding renewal process. Like most electrically stimulated fibers, the conditional mean interval histogram falls within the bounds of the corresponding renewal process at late times. This is consistent the interspike interval being independent of the preceding interval, except when the preceding interval is short. This decorrelation at late times also occurs in the presence of ongoing noise Fig. 10 (j–l).

Supplemental Methods

Here we demonstrate that the numerical methods used in this study produce estimates of the Lyapunov exponent that are robust to errors associated with finite averaging time and finite computational precision. We also demonstrate that the estimates of the Lyapunov exponent exhibit power-law convergence.

The robustness of the finding of dynamical instability in the FN model

Although the two numerical methods used in this study, the NDSolve method and the fixed-step-size Euler method, may make different predictions about a particular solution at late times, even when started with nominally identical initial conditions, we demonstrate that they nevertheless yield similar estimates of the Lyapunov exponent.

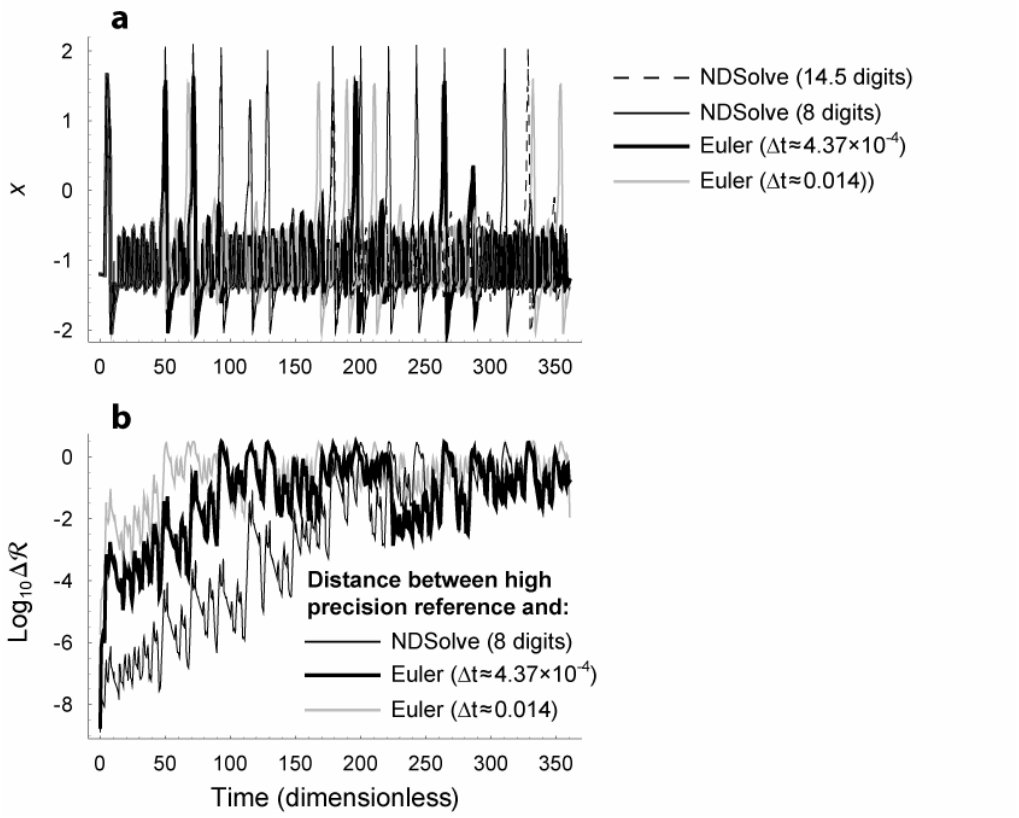

Supplemental Fig. 11. Lower precision solutions diverge from the high-precision solution at similar rates. (a) Time evolution of the excitation variable, x, of the FitzHugh-Nagumo system when driven by a near threshold pulse train (A/A_θ=1.13278) at a rate corresponding to 5 kHz ($T \simeq 3.578$). The different curves correspond to different solution methods (see figure legend). (b) The time evolution of the phase-plane distance between a high-precision solution (14.5 decimal digits) and three lower precision solutions (see figure legend).

Supplemental Figure 11a shows predictions of the voltage-like variable $x(t)$ generated by: 1) the NDSolve algorithm with a high numerical precision setting of 14.5 decimal digits (dashed black line), 2) the NDSolve algorithm with a precision setting of 8 digits that is used for the noise-free simulations in the main text (thin black line), 3) the Euler method with a small step size (thick black line), and 4) the Euler method with the larger step size (gray line) used for the stochastic simulations in the main text. The predictions visually overlap during the first approximately $t \simeq 45$ time units, corresponding to the first 12 pulses, after which the prediction of the larger step-size Euler method noticeably diverges from the other solutions. Later

at $t \simeq 70$ the smaller step-size Euler prediction diverges from the NDSolve solutions. Around $t = 180$ or the 50th pulse, the less precise NDSolve solution diverges from the higher precision NDSolve solution. This behavior is consistent with dynamical instability magnifying the effects of computational error and imprecision.

Supplemental Figure 11b plots the distance $(\Delta\mathcal{R})$ in the phase-plane between the high-precision NDSolve solution and the three lower precision solutions. Consistent with Supplemental Fig. 11a, the phase-plane distance between each of the lower precision solutions and the reference solution increases linearly (on a log scale) as the simulation progresses, with the distance eventually approaching unity (or zero on a log scale). This maximum separation is determined by the width of the attractor in phase space (Fig. 2 of main text). The similar exponential rate of separation of the solutions suggests that the three methods, though differing in their precision, may produce similar estimates of the Lyapunov exponent λ.

Supplemental Figure 12a shows the estimate of the Lyapunov exponent for these three methods as a function of the stimulus duration. The Lyapunov exponent was estimated by solving the FN equations (1) and (2) along with the variational equations (5), as described in the Methods. The total stimulus duration is $t_{total} = 200T + 5NT$, where $T \simeq 3.578$ is the interpulse time. The responses to the initial 200 pulses were discarded to minimize the influence of transients. Five estimates of λ were then made based on the remaining five stimulus segments of length NT. Error bars indicate the standard deviation of the five estimates of the less precise Euler method. This plot shows that even the least precise Euler method produces within 50 time units (14 pulses) an estimate that is significantly greater than zero. The estimates for the later times, along with error bars for all the methods, are shown in Fig. 12b–d. These data suggest that the estimate of the Lyapunov exponent

based on the least precise Euler method converges to a value that is somewhat less than that predicted by the more precise NDSolve algorithm, but that decreasing the step size of the Euler method to $\Delta t = 4.37 \times 10^{-4}$ improves the accuracy of the estimate.

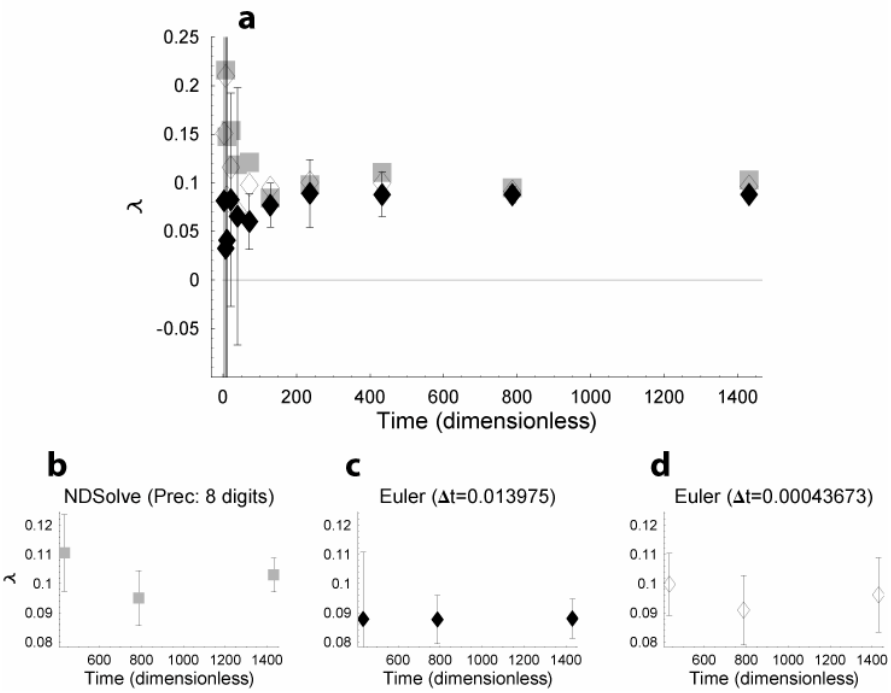

Supplemental Fig. 12. Different solution methods produce similar estimates of the Lyapunov exponent. (a) The mean estimate of the Lyapunov exponent versus the duration of a 5 kHz near threshold (A/A_0=1.13278) pulse train. The different symbols correspond to different solution methods, as in Supplemental Fig. 11. Black diamonds, representing the least precise method, are accompanied by error bars that indicate the standard deviation of estimates based on five sequential pulse trains of duration NT. Panels **b–c** show the Lyapunov exponent estimate versus t at late times, with error bars indicating the standard deviation of five sequential estimates.

While the different procedures appear to converge on slightly different values of λ, the rate at which the estimates converge to these different values is similar. This convergence rate is illustrated in Supplemental Fig. 13 which plots, on logarithmic axes, the standard deviation of the Lyapunov exponent estimate versus the simulation duration t. The approximately linear behavior, with common slopes across methods, suggests that the methods have similar power-law convergence rates.

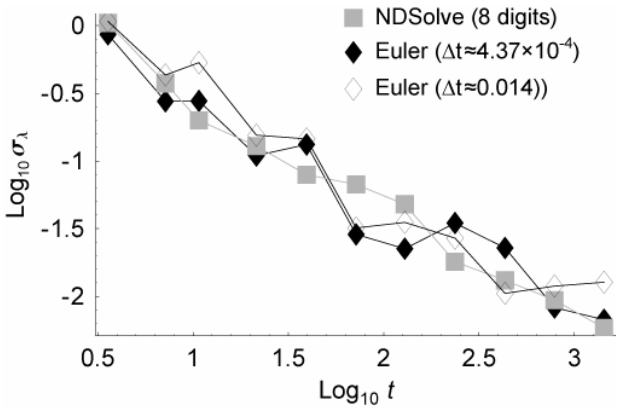

Supplemental Fig. 13. Variability of the Lyapunov exponent estimate decreases with averaging time for three solution algorithms. The logarithm of the standard deviation of the Lyapunov exponent estimate ($\mathrm{Log}_{10}\sigma_\lambda$) as a function of the logarithm of the stimulus duration ($\mathrm{Log}_{10}t$) for three solution methods (see figure legend).

We now further investigate the effects of numerical precision on the estimates using the NDSolve method. The NDSolve method uses an algorithm that adaptively varies the step size in order to achieve the precision goal set by the user. For sufficiently high precision settings, typically above 8 decimal digits, computations must be carried out with a precision greater than the standard machine precision of approximately 16 decimal digits. This higher precision is achieved in *Mathematica* by using arbitrary precision numbers at the expense of longer computation time (Wolfram 1996). Supplemental Figure 14 shows the estimates of λ for $200+5\times300=1700$ pulses for a range of precision settings. Because the mean of every estimate falls within the confidence interval of all the other estimates, we conclude that the finding of instability ($\lambda>0$) is robust to errors in computational precision.

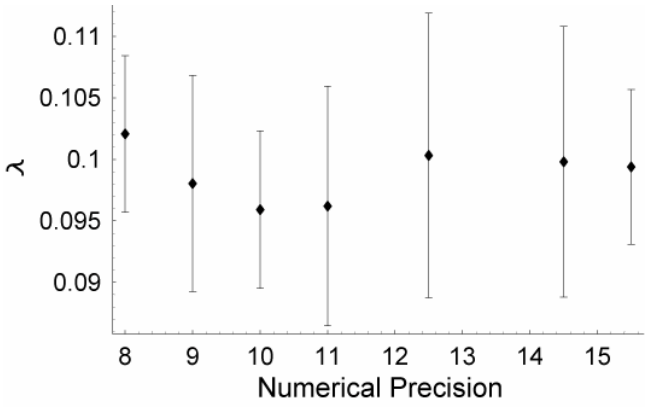

Supplemental Fig. 14. The estimate of the Lyapunov exponent is robust to increases in computational precision. The mean of five estimates of the Lyapunov exponent plotted as a function of the numerical precision setting of the NDSolve algorithm. With a numerical precision of *p*, the local error is less than $10^{-p} + |X_i| 10^{-p}$, where $|X_i|$ is the absolute value of the i^{th} independent variable (Wolfram 1996). The Lyapunov exponent estimates were obtained from pulse trains of duration $NT = 200T + 5 \times 300T = 1700$. The responses to the initial 200 pulses were discarded, and estimates were then formed based on the responses to each of the five subsequent segments consisting of 300 pulses. The error bars represent the standard deviation of these estimates. The stimulus conditions are the same as in Supplemental Figs. 11–13.

In summary, we have shown that for a typical near threshold, high-rate condition both the NDSolve method and the fixed-step-size Euler method predict dynamical instability $(\lambda > 0)$, and further that this prediction of instability is robust to the errors associated with the finite duration and the finite precision of the calculations.

Supplemental Note

For the driven FN model the phase space is, strictly speaking, three dimensional, and thus there are three Lyapunov exponents, one for each dimension (Eckmann and Ruelle 1985). The evolution in this third dimension is given trivially by the equation $t'(t) = 1$ (Strogatz 1994). Along this time axis, there is neither contraction nor stretching, and hence one of the three exponents is identically zero always. Further,

because the system is dissipative, the volume of a small cube of initial conditions will shrink under the influence of the flow. The long-term rate of change in the volume is directly proportional to the sum of the Lyapunov exponents (Eckmann and Ruelle 1985), and, because this volume is contracting, the sum of the exponents must be less than zero, thus when one of the two non-zero exponents is positive the other must be negative. Furthermore, an arbitrary perturbation vector, under the influence of the flow, will seek out the direction of either growth or of slowest contraction (Wolf et al. 1985), thus, the exponent determined by solving the variational equations corresponds to the positive exponent, if there is one, or to the negative exponent which is closest to zero. This exponent we refer to as "the Lyapunov exponent."

References

Eckmann J-P, and Ruelle D. Ergodic theory of chaos and strange attractors. Rev Mod Phys 57: 617-656, 1985.

Hodgkin AL, and Huxley AF. A quantitative description of membrane current and its application to conduction and excitation in nerve. J Physiol (Lond) 117: 500-544, 1952.

Litvak LM, Delgutte B, and Eddington DK. Auditory-nerve fiber responses to electric stimulation: Modulated and unmodulated pulse trains. J Acoust Soc Am 110: 368-379, 2001.

Litvak LM, Smith ZM, Delgutte B, and Eddington DK. Desynchronization of electrically evoked auditory-nerve activity by high-frequency pulse trains of long duration. J Acoust Soc Am 114: 2066-2078, 2003.

Schwarz JR, and Eikhof G. Na currents and action potentials in rat myelinated nerve fibres at 20 and 37 degrees C. Pflugers Arch 409: 569-577, 1987.

Strogatz SH. Nonlinear Dynamics and Chaos. Addison-Wesley, 1994.

Wolf A, Swift JB, Swinney HL, and Vastano JA. Determining Lyapunov exponents from a time series. Physica D 16: 285-317, 1985.

Wolfram S. The Mathematica Book. Wolfram Media/Cambridge University Press, 1996.